Numerical Modeling of Dual-Wavelength Pumped Heavily-Ho^{3+}-Doped Fluoroindate Fiber Lasers With Efficient Output at 3.92 μm

Zhuowei Cheng, Zhi Zhang, Ruicong Wang, Shunbin Wang, Xiaoxu Li, Síle Nic Chormaic, Shijie Jia, and Pengfei Wang

***Abstract*—In this article, laser emission at 3.92 μm in heavily-holmium-doped fluoride fibers using 888 nm and 1660 nm laser as pumping sources is investigated through numerical modeling. The dual-wavelength pumping system has lower threshold and higher slope efficiency than the single-wavelength pumping system at 888 nm. In addition, the system can decrease the heat load due to the 1660 nm input influencing the energy transfer up-conversion and cross-relaxation processes effectively, which indicates the possibility of raising the laser heat-damage threshold and providing high-power 3.92 μm laser generation. This research represents a novel method for improving the performance of 3.92 μm fiber lasers.**

***Index Terms*—DWP, fiber lasers, holmium doped, InF_3 fiber, theoretical analysis.**

I. Introduction

As LASERS with emission at wavelengths longer than 3 μm play an indispensable role in many fields, such as medicine [1], [2], [3], environment [4], and industry [5], [6], [7], they have attracted more and more attention in research. In 1992, H. Többen et al. generated 8 mW of laser output at 3.5μm in erbium-doped ZBLAN fiber using a 655 nm laser as the pump laser [8]. In 2014, O. Henderson-Sapir et al. developed a dual-wavelength (985 nm and 1973 nm) pumping (DWP) system and generated a 3.5μm laser in Er: ZBLAN fiber with an output power of 260 mW [9]. Using this new pumping scheme, the system's efficiency showed an improvement of 16%, by taking advantage of the long-lived $^4I_{11/2}$ state. Two years later, they improved the performance of a 3.5μm laser with output power at the Watt level [5]. In 2021, M. Lemieux-Tanguay. et al. reported a DWP 3.55μm fiber laser with a record output power of 14.9 W [10], demonstrating the advantages of DWP systems compared to single wavelength pumping systems. ZBLAN fiber has been paramount in the successes in fiber laser development in the 3–3.5μm range. However, when the operating wavelength is around 3.9μm, the maximum output power decreases dramatically to 11 mW owing to the relatively high phonon energy of ZBLAN glass, thus limiting the operation of Ho: ZBLAN fiber lasers to cryogenic temperatures, and this is a significant disadvantage that needs to be overcome.

Compared to ZBLAN glass, InF_3-based glass has a lower phonon energy and a longer multiphonon absorption edge. In 2018, Maes et al. demonstrated a 3.92μm fiber laser operating at room temperature with a record output power of 197 mW. by employing Ho^{3+}-doped InF_3-based fiber as the gain medium and an 888 nm laser as the pump. Despite the progress in mid-infrared fiber lasers, the performance of 3.9μm fiber lasers is still far behind that of 3–3.5μm lasers. One fundamental problem is that the 3.9μm transition (Ho^{3+}: $^5I_5 \rightarrow {}^5I_6$) is a self-terminating process since the lifetime of the lower state ($^5I_6$) is much longer than that of the higher state ($^5I_5$). Therefore, exploring a more efficient scheme for generating 3.92μm fiber lasers is crucial.

So far, some efforts have been made to suppress the self-terminating process, which acts as a bottleneck for developing 3.92μm lasers. In 2021, F. Zhou et al. theoretically investigated a new method based on a DWP scheme [11]. The results revealed that a DWP system using 888 nm and 962 nm pump lasers contributed to reducing the system's threshold and effectively enhancing the laser output. In the same year, Loconsole et al. developed a gain-switched pulsed laser using an 8 cm-long section of fluoroindate glass fiber heavily doped with holmium

Manuscript received 23 May 2023; revised 4 July 2023; accepted 11 July 2023. Date of publication 13 July 2023; date of current version 16 November 2023. This work was supported in part by the National Natural Science Foundation of China under Grants 62225502, 61935006, 62090062, 62005060, 61905048, and 62005061, in part by the National Key Research and Development Program of China under Grants 2020YFA0607602 and 2021YFB3500901, in part by the Heilongjiang Provincial Natural Science Foundation of China under Grant LH2020F029, in part by Shenzhen Basic Research Foundation under Grants JCYJ20190808140805488 and JCYJ20190808173619062, in part by 111 Project under Grant B13015, in part by the Fundamental Research Funds for the Central Universities under Grants 3072021CF2514 and 3072021CF2533, and in part by OIST Graduate University. The work of Zhuowei Cheng was supported by Scientific Computing and Data Analysis Section at OIST Graduate University. *(Corresponding author: Pengfei Wang.)*

Zhuowei Cheng, Zhi Zhang, Ruicong Wang, Xiaoxu Li, Shijie Jia, and Pengfei Wang are with the Key Laboratory of In-Fiber Integrated Optics of Ministry of Education, College of Physics and Optoeletronic Engineering, Harbin Engineering University, Harbin 150001, China (e-mail: zhuoweic_98@hrbeu.edu.cn; zhangzhi@hrbeu.edu.cn; wrc@hrbeu.edu.cn; xiaoxuli_99@outlook.com; jiasj@hrbeu.edu.cn; pengfei.wang@tudublin.ie).

Shunbin Wang is with the Qingdao Innovation and Development Center, Harbin Engineering University, Qingdao 266400, China (e-mail: shunbinwang@hrbeu.edu.cn).

Síle Nic Chormaic is with the Light-Matter Interactions for Quantum Technologies Unit, Okinawa Institute of Science and Technology Graduate University, Onna 904-0495, Japan (e-mail: sile.nicchormaic@oist.jp).

Color versions of one or more figures in this article are available at https://doi.org/10.1109/JLT.2023.3295126.

Digital Object Identifier 10.1109/JLT.2023.3295126

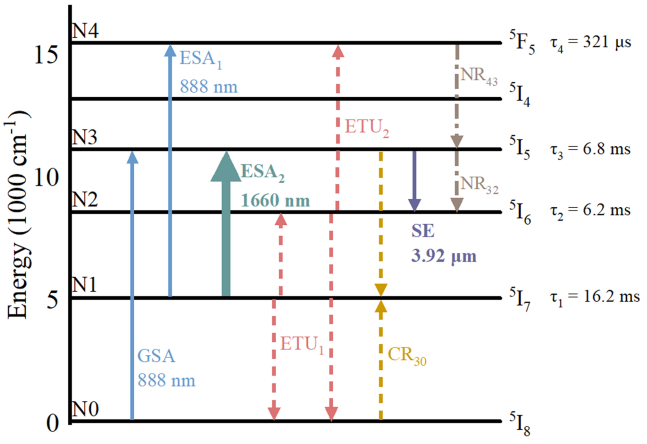

Fig. 1. Energy level diagram of Ho^{3+} GSA: Ground state absorption; ESA: Excited state absorption; ETU: Energy transfer up-conversion; CR: Cross relaxation, SE: Stimulated emission; NR: Nonradiative relaxation.

($N_{\mathrm{Ho}} = 100000$ ppm). The laser was designed to operate with an input peak power of $P_{\mathrm{p}} = 10$ W and a pump repetition rate of f = 100 kHz, resulting in an output signal peak power of approximately $P_{\mathrm{s}} = 14.62$ W at a wavelength of $\lambda = 3.92\mu$m [12]. Subsequently, J. Cao et.al. demonstrated cascade lasing at 3.92μm and 2.92μm, enhancing slope efficiency while reducing the laser threshold and heat accumulation [13]. Meanwhile, the utilization of co-doped fluoroindate glasses has been regarded as a more effective approach for the production of 3.92μm lasers [14], [15], [16]. In a study conducted in 2023, Loconsole et al. employed a nine-level system to simulate the variation of a Ho: Nd-codoped fluoroindate glass fiber. They achieved laser emission at 3.92μm by employing an 808 nm pump laser, resulting in a slope efficiency (η) of 16.67% and an input power threshold (P_{th}) of 0.2 W [17].

In this work, we demonstrate a new DWP method for a 3.92μm fiber laser, using 888 nm and 1660 nm lasers as the pumps. A self-circulatory system is formed in the $^5I_5$, $^5I_6$, and $^5I_7$ levels due to the 1660 nm pumping. This then transports the ions in the $^5I_7$ state to the $^5I_5$ state so that the occupation number of the higher state can be maintained at a high level. Since the pump source of the system is a 1660 nm laser, commercially available high-power lasers can be used. Consequently, this system reduces the threshold and heat accumulation while enhancing the slope efficiency of a 3.92μm fiber laser. Numerical simulations are used to explore the feasibility of this scheme, and the optimal fiber parameters are determined through analysis.

II. Numerical Model

The transition process under consideration in the heavily holmium-doped InF_3 fiber laser is presented in Fig. 1 for a DWP system. The essential processes, including cross-relaxation (CR), nonradiative multiphonon decay (NR), energy transfer upconversion (ETU), ground state absorption (GSA), excited state absorption (ESA) as well as stimulated emission (SE), are shown.

The Ho^{3+}-doped fiber laser can be modeled as a five-energy-level system. Due to large rates of multiphonon relaxation, the population of state $^5I_4$ can be ignored. In the study conducted by [12], the authors also examined the ESA process ($^5I_6 \rightarrow {}^5S_2$) in the gain-switched pulsed laser. However, due to the limitations imposed by the fiber damage threshold, it is not feasible to employ such high pumping powers for the continuous wave (CW) pumping laser. Consequently, the low rate of this ESA process renders it negligible in the overall analysis. The rate equations of the five-energy-level system can be listed as follows [18], [19], [20]:

$$\frac{dN_4(z,t)}{dt} = -\tau_4^{-1}N_4(z,t) - W_{\mathrm{NR43}}N_4(z,t) + R_{\mathrm{ESA1}}(z,t) + R_{\mathrm{ETU2}}(z,t) - R_{\mathrm{SE32}}N_3(z,t) \tag{1}$$

$$\frac{dN_3(z,t)}{dt} = \beta_{43}N_4(z,t) + W_{\mathrm{NR43}}N_4(z,t) - R_{\mathrm{SE32}}N_3(z,t) - \tau_3^{-1}N_3(z,t) - W_{\mathrm{NR32}}N_3(z,t) + R_{\mathrm{ESA2}}(z,t) + R_{\mathrm{GSA}}(z,t) - R_{\mathrm{CR30}}(z,t) \tag{2}$$

$$\frac{dN_2(z,t)}{dt} = \sum_{i=3,4}\beta_{i2}\tau_i^{-1}N_i(z,t) + W_{\mathrm{NR32}}N_3(z,t) - \tau_2^{-1}N_2(z,t) + R_{\mathrm{SE32}}(z,t) + R_{\mathrm{ETU1}}(z,t) - 2R_{\mathrm{ETU2}}(z,t) \tag{3}$$

$$\frac{dN_1(z,t)}{dt} = \sum_{i=2,3,4}\beta_{i1}\tau_i^{-1}N_i(z,t) - \tau_1^{-1}N_1(z,t) - R_{\mathrm{ESA1}}(z,t) - R_{\mathrm{ESA2}}(z,t) + 2R_{\mathrm{CR30}}(z,t) - 2R_{\mathrm{ETU1}}(z,t) \tag{4}$$

$$N_{\mathrm{Ho}}(z,t) = \sum_{i=0,1,2,3,4} N_i(z,t) \tag{5}$$

where N_i is the population density of ions in level i, β_{ij} is the luminescence branching ratio, and τ_i is the radiative lifetime of the excited states of Ho^{3+} (labeled as i = 1, 2, 3, and 4). The rates of NR processes are $W_{\mathrm{NR43}} = 58234\ \mathrm{s}^{-1}$ and $W_{\mathrm{NR32}} = 7260\ \mathrm{s}^{-1}$, respectively [18]. The ETU rates R_{ETU1} and R_{ETU2} can be defined as

$$R_{\mathrm{ETU1}}(z,t) = W_{11}N_1^2(z,t) \tag{6}$$

$$R_{\mathrm{ETU2}}(z,t) = W_{22}N_2^2(z,t) \tag{7}$$

where W_{11} and W_{22} represent the parameters of the ETU_1 and ETU_2 processes. The cross-relaxation rate of R_{CR30} is given by

$$R_{\mathrm{CR30}}(z,t) = W_{30}(z,t)N_3(z,t)N_0(z,t) \tag{8}$$

where W_{30} is the cross-relaxation parameter. Meanwhile, the GSA, ESA_1 and ESA_2 pump rates R_{GSA}, R_{ESA1} and R_{ESA2} can be defined as follows [21]:

$$R_{\mathrm{GSA}}(z,t) = \frac{\lambda_{\mathrm{p1}}\Gamma_{\mathrm{p1}}}{hcA_{\mathrm{core}}}\left[\sigma_{\mathrm{GSA03}}N_0(z,t) - \sigma_{\mathrm{EMI30}}N_3(z,t)\right] \times \left[P_{\mathrm{p1}}^{+}(z,t) + P_{\mathrm{p1}}^{-}(z,t)\right] \tag{9}$$

$$R_{\mathrm{ESA1}}(z,t) = \frac{\lambda_{\mathrm{p1}}\Gamma_{\mathrm{p1}}}{hcA_{\mathrm{core}}}\left[\sigma_{\mathrm{ESA14}}N_1(z,t) - \sigma_{\mathrm{EMI41}}N_4(z,t)\right] \times \left[P_{\mathrm{p1}}^{+}(z,t) + P_{\mathrm{p1}}^{-}(z,t)\right] \tag{10}$$

$$R_{\mathrm{ESA2}}(z,t)=\frac{\lambda_{\mathrm{p2}}\Gamma_{\mathrm{p2}}}{hcA_{\mathrm{core}}}\left[\sigma_{\mathrm{ESA13}}N_1(z,t)-\sigma_{\mathrm{EMI31}}N_3(z,t)\right]\times\left[P_{\mathrm{p2}}^{+}(z,t)+P_{\mathrm{p2}}^{-}(z,t)\right] \quad (11)$$

where λ_{p1} and λ_{p2} are the 888 nm and 1660 nm pump wavelengths, respectively. Γ_{p1} denotes the power filling factor for 888 nm light and can be estimated as the ratio of the core cross-sectional area A_{core} to the cladding cross-sectional area A_{clad}. h is Planck's constant; c is the speed of light in a vacuum. σ_{GSA03}, σ_{ESA14} and σ_{ESA13} are the GSA and ESA$_1$ and ESA$_2$ absorption cross-sections, respectively. σ_{EMI30}, σ_{EMI41} and σ_{EMI31} are the GSA, ESA$_1$ and ESA$_2$ corresponding emission cross-sections, respectively. $P_{p1}^{+}(x,t)$ and $P_{p1}^{-}(x,t)$ denote the forward and backward propagating pump power at 888 nm, while $P_{p2}^{+}(x,t)$ and $P_{p2}^{-}(x,t)$ represent the forward and backward pump power at 1660 nm. The rate of stimulated emission R_{SE32} for the 3.92μm emission is

$$R_{\mathrm{SE32}}(z,t)=\frac{\lambda_{\mathrm{s}}\Gamma_{\mathrm{s}}}{hcA_{\mathrm{core}}}\left[\sigma_{\mathrm{EMI32}}N_3(z,t)-\sigma_{\mathrm{ABS23}}N_2(z,t)\right]\times\left[P_{\mathrm{s}}^{+}(z,t)+P_{\mathrm{s}}^{-}(z,t)\right] \quad (12)$$

where λ_{s} is the signal wavelength for the $^5\mathrm{I}_5\rightarrow{}^5\mathrm{I}_6$ transition. σ_{EMI32} and σ_{ABS23} are the effective cross-sections of emission and absorption for the $^5\mathrm{I}_5\rightarrow{}^5\mathrm{I}_6$ transition, respectively, and can be calculated by:

$$\sigma_{\mathrm{EMI32}}=b_3\sigma_{\mathrm{SE32}} \quad (13)$$

$$\sigma_{\mathrm{ABS32}}=\frac{g_3}{g_2}b_2\sigma_{\mathrm{SE32}} \quad (14)$$

where σ_{SE32} is the emission cross-section, b_2 and b_3 are the Boltzmann factors, and g_2, g_3 are the higher and lower laser sublevel degeneracies. $P_s^{+}(x,t)$ and $P_s^{-}(x,t)$ denote the forward and backward propagating signal powers for the 3.92μm emission. Γ_{s} represents the power filling factor for the 3.92μm laser propagating in the fiber core. The light is assumed to have a Gaussian distribution; thus it can be calculated from [19]:

$$\Gamma_{\mathrm{s}}\approx 1-\exp\left(-2\frac{d_{\mathrm{core}}^2}{\omega_0^2}\right) \quad (15)$$

where d_{core} is the fiber core radius, and ω_0 is the mode field radius. ω_0 is estimated for single-mode and step-index fibers using the Marcuse empirical formula [18]:

$$\omega_0=d_{\mathrm{core}}\left(0.65+1.619V^{-1.5}+2.879V^{-6}\right) \quad (16)$$

where the normalized frequency V can be calculated by $2\pi r_{\mathrm{core}}$ $NA/\lambda_{\mathrm{SE32}}$ and NA is the numerical aperture of the fiber. A schematic of the setup of the DWP system is shown in Fig. 2. The evolution of optical power is defined by the following equations [11]:

$$\pm\frac{dP_{\mathrm{SE32}}^{\pm}(z,t)}{dz}=\Gamma_{\mathrm{S}}\left[\sigma_{\mathrm{EMI32}}b_3N_3(z,t)-\frac{g_3}{g_2}b_2\sigma_{\mathrm{ABS23}}N_2(z,t)\right]\times P_{\mathrm{SE32}}^{\pm}(z,t)-\alpha_{\mathrm{S}}P_{\mathrm{SE32}}^{\pm}(z,t) \quad (17)$$

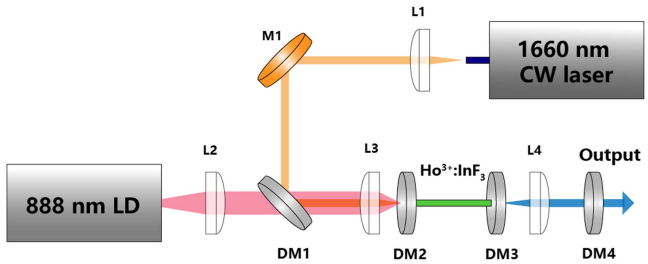

Fig. 2. Schematic of the Ho^{3+}: InF$_3$ fiber laser. L1–L4, lenses; M1, gold-sputtered mirror; DM1–DM4, dichroic mirror. Two pump lasers are shown at 1660 nm and 888 nm.

$$\pm\frac{dP_{\mathrm{P1}}^{\pm}(z,t)}{dz}=-\Gamma_{\mathrm{P1}}[\sigma_{GSA03}N_0(z,t)-\sigma_{\mathrm{EMI30}}N_3(z,t)+\sigma_{\mathrm{ESA14}}N_0(z,t)-\sigma_{\mathrm{EMI41}}N_3(z,t)]\times P_{\mathrm{P1}}^{\pm}(z,t)-\alpha_{\mathrm{P1}}P_{\mathrm{P1}}^{\pm}(z,t) \quad (18)$$

$$\pm\frac{dP_{\mathrm{P2}}^{\pm}(z,t)}{dz}=\Gamma_{\mathrm{P2}}\left[\sigma_{\mathrm{ESA13}}N_1(z,t)-\sigma_{\mathrm{EMI31}}N_3(z,t)\right]\times P_{\mathrm{P2}}^{\pm}(z,t)-\alpha_{\mathrm{P2}}P_{\mathrm{P2}}^{\pm}(z,t), \quad (19)$$

where α_{P1} and α_{P2} are the background loss coefficients for 888 nm and 1660 nm pump light, respectively, and α_{s} is the background loss coefficient at the signal wavelength. The boundary conditions for the pump power and laser power at both ends of the fiber can be defined as follows:

$$P_{\mathrm{P1}}^{+}(0,t)=R_{03\mathrm{f}}P_{\mathrm{P1}}^{-}(0,t)+P_{\mathrm{P1,Launch}}(0,t) \quad (20)$$

$$P_{\mathrm{P1}}^{-}(L,t)=R_{03\mathrm{b}}P_{\mathrm{P1}}^{+}(L,t) \quad (21)$$

$$P_{\mathrm{P2}}^{+}(0,t)=R_{13\mathrm{f}}P_{\mathrm{P2}}^{-}(0,t)+P_{\mathrm{P2,Launch}}(0,t) \quad (22)$$

$$P_{\mathrm{P2}}^{-}(L,t)=R_{13\mathrm{b}}P_{\mathrm{P2}}^{+}(L,t) \quad (23)$$

$$P_{\mathrm{SE32}}^{+}(0,t)=R_{32\mathrm{f}}P_{\mathrm{SE32}}^{-}(0,t) \quad (24)$$

$$P_{\mathrm{SE32}}^{-}(L,t)=R_{32\mathrm{b}}P_{\mathrm{SE32}}^{+}(L,t) \quad (25)$$

where $R_{03\mathrm{f}}$ and $R_{03\mathrm{b}}$ represent the input and output mirror reflectivity for the 888 nm pump source, respectively. $R_{13\mathrm{f}}$ and $R_{13\mathrm{b}}$ are the input and output mirror reflectivity for the 1660 nm pump source. L is the fiber length. $P_{\mathrm{P1,\ Launch}}$, and $P_{\mathrm{P2,\ Launch}}$ denote the launched pump power at 888 nm and 1660 nm, respectively. $R_{32\mathrm{f}}$ and $R_{32\mathrm{b}}$ represent the reflectivity of the front mirror and output mirror for the 3.92μm signal.

III. Simulation Parameters

Most of the values of the parameters used in this work are from published works. Only a few articles provide experimental values for the spectral parameters of Ho^{3+}-doped fluoride glass fibers, and some parameters have yet to be experimentally measured. In this case, we determine them by speculation, approximation, or fitting in this work.

The intrinsic lifetimes and the corresponding branching ratios of the investigated states are listed in Table I. The values of the lifetimes of levels 1–4 and their corresponding branching ratios are taken from [1].

TABLE I
SUMMARY OF THE VALUES OF THE EXCITED-STATE LIFETIMES AND BRANCHING RATIOS OF Ho^{3+} IN InF_3 HOST

Symbol	Values	Description
τ_1	16.2 ms	$^5I_7$ radiative life time
τ_2	6.2 ms	$^5I_6$ radiative life time
τ_3	6.8 ms	$^5I_5$ radiative life time
τ_4	321 μs	$^5F_5$ radiative life time
β_{10}	1	branching ratio $^5I_7 \rightarrow {}^5I_8$
β_{21}, β_{20}	0.058,0.942	branching ratio $^5I_6 \rightarrow {}^5I_7$, $^5I_6 \rightarrow {}^5I_8$
$\beta_{32}, \beta_{31}, \beta_{30}$	0.013,0.430,0.557	branching ratio $^5I_5 \rightarrow {}^5I_6$, $^5I_5 \rightarrow {}^5I_7$, $^5I_5 \rightarrow {}^5I_8$
$\beta_{43}, \beta_{42}, \beta_{41}, \beta_{40}$	0.004,0.046,0.192, 0.758	branching ratio $^5F_5 \rightarrow {}^5I_5$, $^5F_5 \rightarrow {}^5I_6$, $^5F_5 \rightarrow {}^5I_7$, $^5F_5 \rightarrow {}^5I_8$
W_{NR10}	0	Non-radiative rates $^5I_7 \rightarrow {}^5I_8$
W_{NR21}	0	Non-radiative rates $^5I_6 \rightarrow {}^5I_7$
W_{NR32}	7260 s^{-1}	Non-radiative rates $^5I_5 \rightarrow {}^5I_6$
W_{NR43}	58234 s^{-1}	Non-radiative rates $^5F_5 \rightarrow {}^5I_5$

TABLE II
SUMMARY OF THE SPECTRUM PARAMETERS

Symbol	Values	Description
λ_{p1}	888 nm	Wavelengths of pumping and signal power
λ_{p2}	1660 nm	
λ_s	3920 nm	
σ_{GSA03}	4.3×10^{-26} m^2	Absorption cross section $^5I_8 \rightarrow {}^5I_5$
σ_{EMI30}	4.6×10^{-26} m^2	Emission cross section $^5I_5 \rightarrow {}^5I_8$
σ_{ESA14}	3.5×10^{-25} m^2	Absorption cross section $^5I_7 \rightarrow {}^5F_5$
σ_{ESA13}	1.18×10^{-25} m^2	Absorption cross section $^5I_7 \rightarrow {}^5I_5$
σ_{EMI31}	1.61×10^{-25} m^2	Emission cross section $^5I_5 \rightarrow {}^5I_7$
σ_{SE32}	3.4×10^{-25} m^2	Emission cross section $^5I_5 \rightarrow {}^5I_6$
b_2	0.32	Boltzmann factors
b_3	0.24	
g_2	13	sublevel degeneracies
g_3	11	

The pump and signal light parameters are listed in Table II, which contains the wavelengths of a pump (888 nm, 1660 nm) and signal (3.92μm) lights, as well as the effective absorption and emission cross-sections used in the simulation. The GSA cross-section σ_{GSA03} and ESA_1 cross-section σ_{ESA14} of P_1 and the emission cross-section σ_{EMI32} have been presented in previous works [11]. The unknown emission cross-sections are determined by measuring them for our custom-fabricated Ho^{3+}-doped fluoride glass. The cross-section of the corresponding absorption process of ESA_2 can be calculated from the emission cross-section using the McCumber theory [18]:

$$\sigma_{ABS}(\lambda) = \sigma_{EMI}(\lambda)\frac{N_u}{N_l}\exp\left(\frac{-\hbar\omega}{k_B T}\right) \tag{26}$$

where σ_{EMI} and σ_{ABS} are the cross-sections of emission and absorption at wavenumber ν for the transition between a lower level i and a higher level j, k_B is Boltzmann's constant, T is the temperature that is assumed to be 300 K ($k_B T = 207$ cm^{-1}). $\hbar\omega$ is the emission photon energy (in cm^{-1}), $N_i = g_i \exp(E_i/(k_B T))$ and N_l is the equilibrium population at $T = 300$ K for the initial state (i.e., $^5I_7$ at $E_1 = 5116$ cm^{-1}) and N_u is the final state (i.e., $^5I_5$ at $E_2 = 11165$ cm^{-1}). The term g_i is the i-level degeneracy

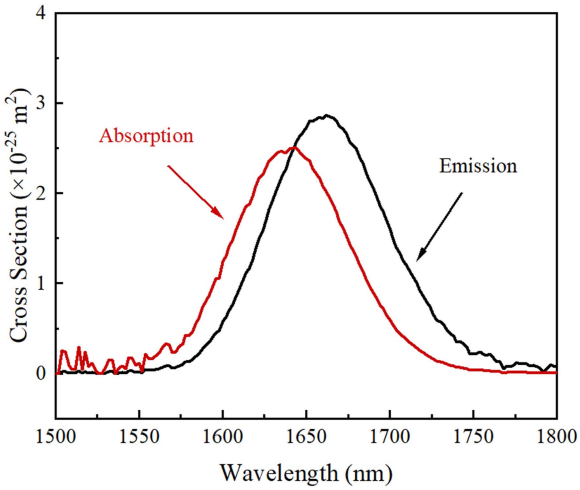

Fig. 3. Calculated absorption (σ_{ESA13}, red curve) and emission (σ_{EMI31}, black curve) cross-section of the transitions between $^5I_7$ and $^5I_5$ state.

TABLE III
SUMMARY OF THE FIBER PARAMETERS

Symbol	Values	Description
L	To be optimized	Fiber length
d_{core}	8 μm	Diameters of core and clad
d_{clad}	45 μm	
NA	0.2	Numerical aperture
α_s	0.2 dB m^{-1}	Fiber loss at 3.92 μm
α_{p1}	0.42 dB m^{-1}	Fiber loss at 888 nm
α_{p2}	1 dB m^{-1}	Fiber loss at 1660 nm
N_{Ho}	2×10^{27} m^{-3}	Ions concentration
R_{03f}	13%	Front lens reflection index at 888 nm
R_{03b}	15%	Back lens reflection index at 888 nm
R_{13f}	4%	Front lens reflection index at 1660 nm
R_{13b}	4%	Back lens reflection index at 1660 nm
R_{32f}	99%	Front lens reflection index at 3.92 μm
R_{32b}	To be optimized	Back lens reflection index at 3.92 μm

with values $g_l = 15$ for the $^5I_7$ state and $g_u = 11$ for the $^5I_5$ state. The spectra of the calculated cross-sections are shown in Fig. 3. The Ho^{3+} ions concentration of the glass used in this work is $N_{Ho} = 15000$ ppm, so the value of the cross-section may deviate from the true values of heavily doped Ho^{3+} glass.

The parameters used in our simulations are shown in Table III. These are mainly from the previous experiment using the single 888 nm pumping [22]. The radius of the core and cladding of the fiber is 8μm and 45μm, respectively. The fiber has a numerical aperture (NA) of 0.2. The fiber losses are 0.2 dB/m at 3.92μm and 0.42 dB/m at 888 nm. The Ho^{3+} doping concentration in InF_3 fiber is 100000 ppm, and the corresponding density is 2×10^{27} m^{-3}. The input and output mirror reflectivities at 1660 nm pump light R_{P2_1} and R_{P2_2} are assumed to be 4%.

IV. VALIDATION

Firstly, the simulation results in this work are supposed to be compared with the experimental results of previous literature. Reference [23] calculated the ETU and CR parameters W_{ETU1},

TABLE IV
SUMMARY OF THE INTERIONIC PARAMETERS

Symbol	Values	Description
W_{11}	1.85×10^{-23} m^3 s^{-1}	ETU rate: $^5I_7 \rightarrow {}^5I_6$, $^5I_7 \rightarrow {}^5I_8$
W_{22}	3.85×10^{-23} m^3 s^{-1}	ETU rate: $^5I_6 \rightarrow {}^5F_5$, $^5I_6 \rightarrow {}^5I_8$
W_{30}	1.10×10^{-24} m^3 s^{-1}	CR rate: $^5I_5 \rightarrow {}^5I_7$, $^5I_8 \rightarrow {}^5I_7$

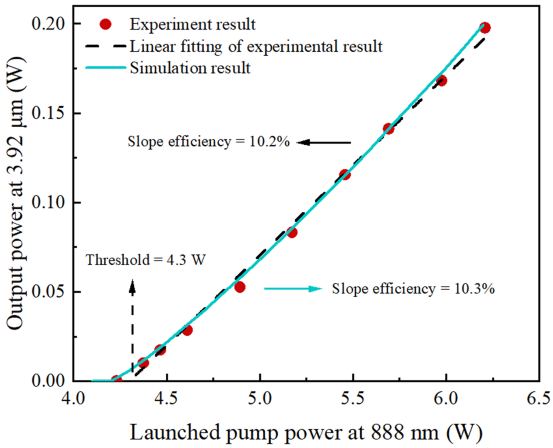

Fig. 4. Simulated and experimental laser output power as functions of launched pump power.

W_{ETU2}, and W_{CR} with the unit of s^{-1}. There is a method from [24] to transfer the interionic parameters unit from s^{-1} to m^3s^{-1}. Using $W_{11} = W_{\mathrm{ETU1}}/N_{\mathrm{S1}}$ and $W_{22} = W_{\mathrm{ETU2}}/N_{\mathrm{S2}}$, the ETU and CR parameters can be obtained, where N_{S1} and N_{S2} are their critical excited densities. However, the values were measured in 10 mol% Ho^{3+}-doped InF_3 glass. As is known from the previous reports about Er^{3+}-doped and Ho^{3+}-doped ZBLAN fiber lasers [25], the ETU and CR parameters in the fiber are usually lower than the bulk glass test results. These two sets of parameters are called weakly interacting (WI) and strong interacting (SI) parameters, and there is a certain ratio between them. The SI parameters values of W_{ETU1}, W_{ETU2} and W_{CR} were calculated to be 1.27×10^{-22} m^3 s^{-1}, 2.1×10^{-22} m^3 s^{-1}, and 3.48×10^{-23} m^3 s^{-1}, respectively. The calculated WI parameters used in this simulation are shown in Table IV (marked as Cal. in the table) to get the best agreement between the simulation and experimental results.

Fig. 4 presents the experimental data linear fitting and simulation result. The simulated laser threshold and slope efficiency are 4.3 W and 10.3%, respectively. Both are close to the experimental results reported in reference [11], in which the threshold is 4.3 W, and the slope efficiency is 10.2%, respectively.

The consistency with the previous results of a single 888 nm wavelength pump experiment proves the validity of the simulation in this work. On this basis, this simulation model can be used to predict the performance of 3.92μm fiber laser.

V. SIMULATION RESULTS

Since a larger pump power requires a smaller step size, the operation time will be greatly increased, when P_2 reaches 6 W, a single operation takes several days, so we only take P_2 = 5W at most in this work. Fig. 5(a) shows that the output power of a 3.92μm fiber laser varies with pump power at 888 nm P_1 when the pump power at 1660 nm P_2 is fixed at 1–5 W. The output power when P_2 is switched off is also given. Increasing the 1660 nm pump power can significantly decrease the laser threshold. Moreover, the threshold approaches zero when the pump power at 1660 nm is set as 5 W. This phenomenon can be ascribed to the ESA_2 process, which transports $^5I_7$ state ions to the $^5I_5$ state and consequently decreases the rate of the ETU_1 process. In addition, the population density of the $^5I_6$ state decreases while the population density of the $^5I_5$ state increases. This process finally leads to a more significant inversion population and increases output power. In the following preliminary assumption, the 2.92μm cascade system formed by

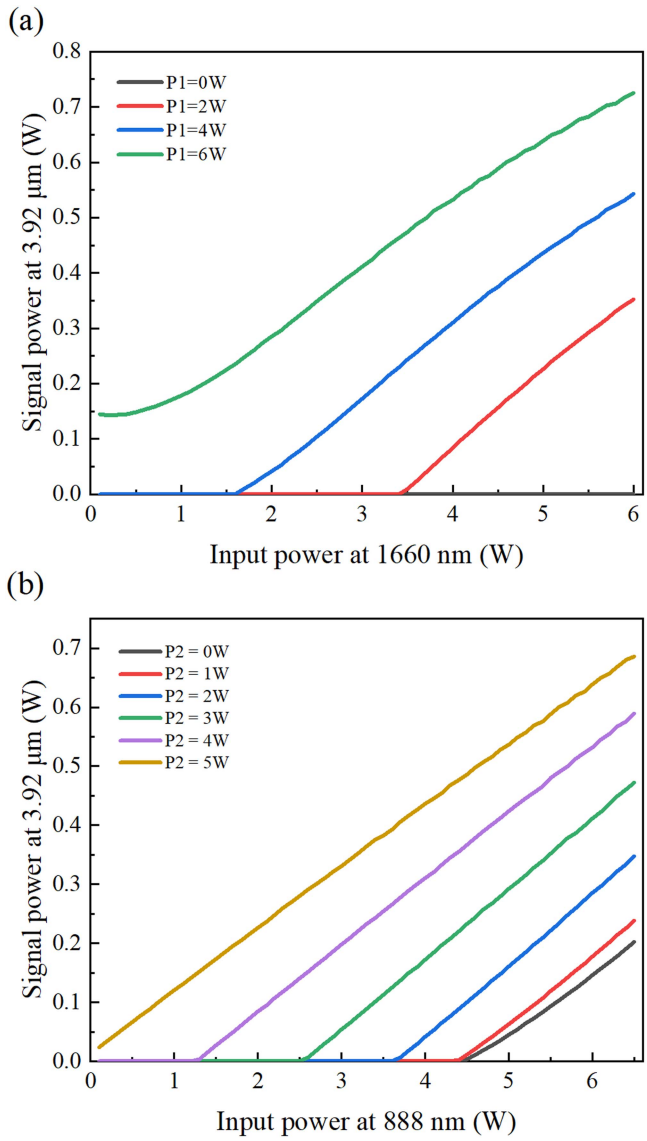

Fig. 5. Simulated 3.92μm signal output in the dual-wavelength pumping system when fiber length is fixed at 0.2 m and back lens reflection index at 3.92μm is fixed at 0.84. (a) Laser output as a function of P_2 when P_1 is fixed at 0, 2, 4, 6 W. (b) Laser output as a function of P_1 when P_2 is fixed at 0–5 W.

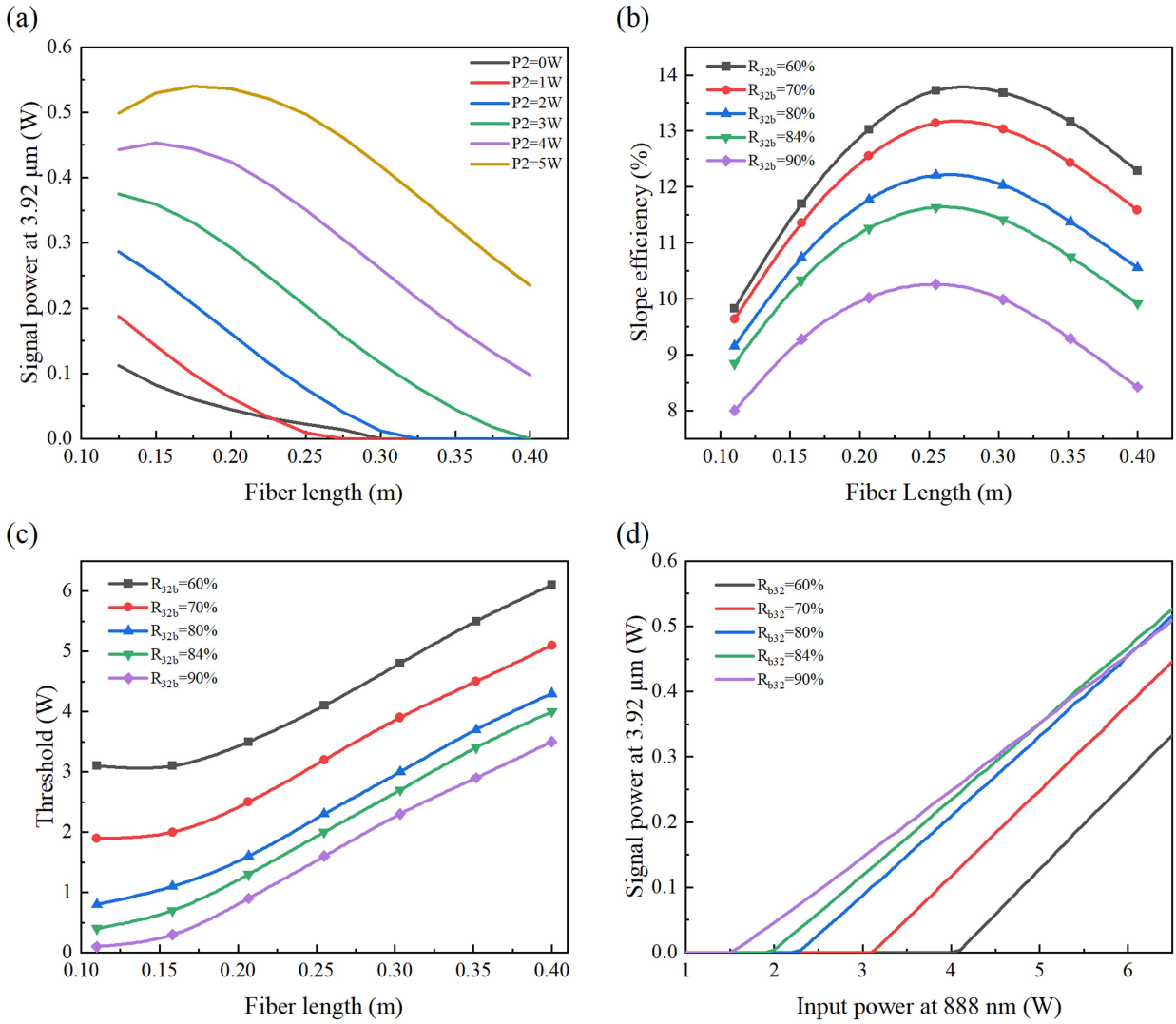

Fig. 6. Simulated result in the dual-wavelength pumping system. (a). Signal output as a function of fiber length when P_1 is fixed at 6.5 W, R_{32b} is fixed at 84% and P_2 is varied from 0 TO 5 W. (b) Slope efficiency as a function of fiber length when P_1 is fixed at 6.5 W, P_2 is fixed at 5 W, and R_{32b} is varied from 60%–90%. (c). Threshold as a function of fiber length when P_1 is fixed at 6.5 W, P_2 is fixed at 5 W, and R_{32b} is varied from 60%–90%. (d). Laser output as a function of P_1 when P_2 is fixed at 5 W, fiber length is fixed at 0.2 m and R_{32b} is varied from 60%–90%.

the 2.92μm mirror or FBGs may enhance the 1660 nm pumped self-circulation system. This topic will be studied in the future.

Based on this, we performed a series of optimization simulations on the DWP system to improve the efficiency and output power of the 3.92μm fiber laser. Fig. 5(b) shows that the output power of the 3.92μm fiber laser varies with P_2 when P_1 is fixed at 0 W, 2 W, 4 W, and 6 W. We observe that the influence of the 1660 nm laser increases with increasing 888 nm laser pump power. Meanwhile, we see that, with an increasing pump power of the 1660 nm laser, the slope efficiency first increases and then decreases to zero gradually. The reason for this is that the rate at which the $^5I_7$ state accumulates is lower than the rate at which the 1660 nm laser dissipates. If P_1 and P_2 are set to 6 W, the 3.92μm laser output power will be 0.54 W.

In Fig. 6(a), we see that when the pump power of the 888 nm laser is fixed at 4 W, the optimal fiber length increases with increasing pump power of the 1660 nm laser. When the power of the 1660 nm pump reaches 5 W, the maximum output power of the 3.92μm fiber laser reaches 0.54 W with a fiber length of 0.175 m. As we can see from Fig. 6(a), in the case of the same pump power at 888 nm P_1, when pump power at 1660 nm P_2 is turned on, the dependence of the 3.92μm laser concerning fiber length becomes more evident. This phenomenon is because the 1660 nm pump laser helps to enhance the absorption of the 888 nm pump light. Simulations for different conditions were performed to verify the influence of the 1660 nm pump laser on the 3.92μm fiber laser. In one, we switched off the ESA_2 process by fixing P_2 at 0 W, termed "ESA_2 off". On the other, we switched on the ESA_2 process by fixing P_2 at 5 W, termed "ESA_2 on". We found that the unabsorbed power of the 888 nm laser for "ESA_2 on" is less than that for "ESA_2 off".

Based on this, the fiber length of the DWP system is optimized when the 1660 nm pump power P_2 is fixed at 5 W. Fig. 6(b) and (c) show how the laser output threshold and slope efficiency vary with the fiber length when the output coupling reflectance is 60%–90%, and 84%, respectively. Due to the high doping

concentration, the optimal length of the fiber is 20–30 cm. The threshold value decreases with increased output coupling reflectivity while the slope efficiency decreases. To further discuss the effect of output reflectivity on the output power of the 3.92μm laser, the relationship between P_1 and P_2 was studied with the mirror's reflectance at the end of the fiber R_{32b} fixed. The 3.92μm output power as a function of 888 nm pump power is shown in Fig. 6(d). The output power reaches 0.526 W when the output coupling reflectance is 84%, pump power $P_1 = 6.5$ W and $P_2 = 5$ W, respectively. From this curve, we conclude that a higher reflectance contributes to a lower threshold but results in low slope efficiency. The optimal reflectance range is between 80–90% when the input power is lower than 10 W. A lower reflectance enables high-power laser output in the high-power pumping system when the pump power of 888 nm is more significant than 6 W.

It was mentioned in [26] that the fiber cavity failed under a high-power input condition because of too much heat load at the butt-coupling between the fiber and the entrance DM1. To explore whether our DWP system helps reduce the heat load on the fiber, we studied the relationship between the fiber heat load and the 1660 nm pump power. The heat load was calculated by considering the nonradiative decay from the excited states and the exothermic or endothermic heat generated by Energy Transfer (ET) processes according to [13]:

$$q = A_{\text{core}} \left(\sum_{i=1}^{6} N_i W_{\text{NR}ij} \left(E_i - E_j \right) + \sum_{\text{ET}} W_{ij} N_i N_j \delta_{ij} \right) \tag{27}$$

where q is the heat load generated per unit length (W/m), A_{core} is the area of the fiber core (m^2), N_i is the population density in level i (m^{-3}), $W_{\text{NR}ij}$ is the nonradiative decay rate of level i. δE_{ij} and E_i are the exothermic or endothermic energy of ET W_{ij} and energy of level i, respectively. The ET processes in this work are ETU_1, ETU_2, and CR, W_{ij} represents the rate of ET process. Heat loads at $x = 0$ as a function of 1660 nm pump power when the reflectance of the mirror in the end of the fiber is fixed at 84%, fiber length $L = 0.2$ m, and pump power at 888 nm P_1 is set as 6.2 W are shown in Fig. 7. The heat load in the fiber is effectively reduced when the 1660 nm pump power is increased. This may be due to the decrease of the energy-endothermic of the ET process rates with the increase to pump power at 1660 nm P_2. To confirm this conjecture, the ET processes as a function of 1660 nm input power are shown in Fig. 8. The ET rates decrease with an increase in the launched 1660 nm pump power.

However, the 3.9μm laser output generated by the designed pumping system still cannot exceed 1W. As can be hypothesized from Fig. 5(a), this may be due to the accumulation of too many $^5I_6$ level particles, resulting in the continuous increase of 1660 nm laser without more $^5I_7$ level particles being promoted to $^5I_5$ level. The resulting higher 1660nm pump power also does not enable laser enhancement. If the new co-doping scheme is adopted [17] in the subsequent work and the cascade system [11] is used, the efficiency will be improved even more.

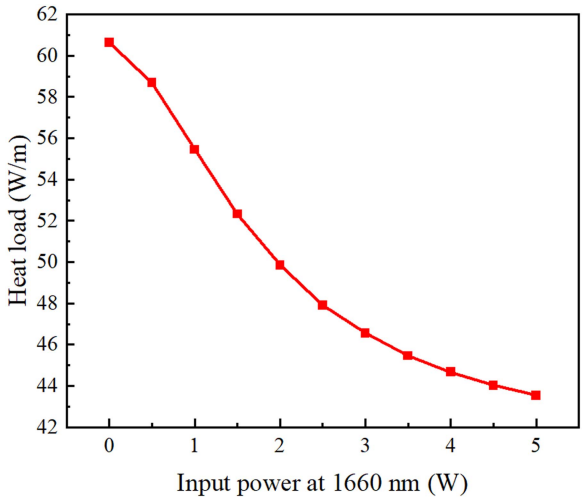

Fig. 7. Calculated heat load in fiber at x = 0 as a function of pump powers at 1660 nm when $R_{32b} = 84\%$, L = 0.2 m, and P_1 is fixed as 6.2 W.

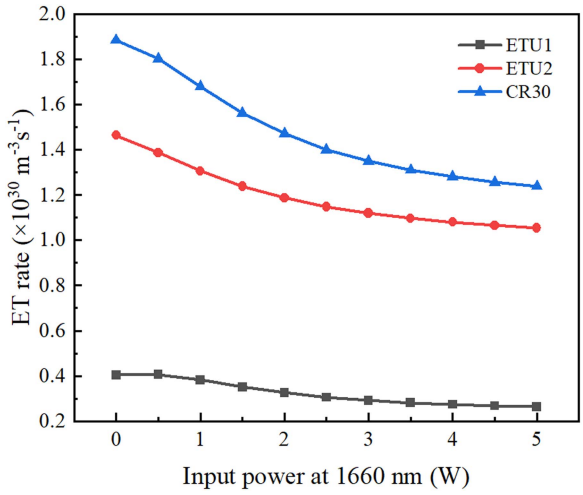

Fig. 8. ET rates as a function of input power at 1660 nm when $R_{32b} = 84\%$, L = 0.2 m, and P_1 is fixed as 6.2 W.

VI. Conclusion

In this work, we demonstrate a new DWP system to generate a 3.92μm laser with at most greater efficiency, lower threshold of about 2 W, and higher slope efficiency of about 12.1% than the conventional 888 nm single-wavelength pumping system. This is due to the self-circulatory system produced by the 1660 nm ESA_2 process, which plays a significant part in maintaining the population inversion of the 3.92μm transition. In this system, the nonradiative process effectively influences the ESA_2 process, which decreases the rate of the ETU_1 process. A decrease in the population of the $^5I_7$ state due to the ESA_1 avoids the accumulation of population in the $^5I_6$ state. Correspondingly, this also increases the rate of the ETU_2 process. In highly Ho^{3+} doped glass, the ETU_2 process strongly transports ions from $^5I_6$ to $^5F_5$ and $^5I_8$, thereby perfectly solving the problem of particle accumulation in the $^5I_6$ state [27]. Compared to single-wavelength pumping, the DWP system is more efficient at maintaining the population inversion. In addition, we showed that the 1660 nm

laser could effectively reduce the heat load of Ho^{3+}: InF_3 fiber. One possible limitation is that the cross-relaxation process will prevent the formation of a higher population in the $^5I_5$ state. This is especially noticeable in glasses with a higher concentration of dopants, specifically those exceeding 10 mol%. In order to solve this problem, cascaded systems are recommended. Our results will be confirmed through experiments in the future. This new scheme could provide significant practical guidance for designing a DWP system for 3.92μm laser output.

REFERENCES

[1] R. R. Anderson et al., "Selective photothermolysis of lipid-rich tissues: A free electron laser study," *Lasers Surg. Med.: J. Amer. Soc. Laser Med. Surg.*, vol. 38, no. 10, pp. 913–919, 2006.

[2] M. C. Pierce, S. D. Jackson, M. R. Dickinson, T. A. King, and P. Sloan, "Laser-tissue interaction with a continuous wave 3-μm fibre laser: Preliminary studies with soft tissue," *Lasers Surg. Med.: J. Amer. Soc. Laser Med. Surg.*, vol. 26, no. 5, pp. 491–495, 2000.

[3] G. M. Peavy, L. Reinisch, J. T. Payne, and V. Venugopalan, "Comparison of cortical bone ablations by using infrared laser wavelengths 2.9 to 9.2μm," *Lasers Surg. Med.: J. Amer. Soc. Laser Med. Surg.*, vol. 25, no. 5, pp. 421–434, 1999.

[4] S. D. Jackson, "Towards high-power mid-infrared emission from a fibre laser," *Nature Photon.*, vol. 6, no. 7, pp. 423–431, 2012.

[5] O. Henderson-Sapir, A. Malouf, N. Bawden, J. Munch, S. D. Jackson, and D. J. Ottaway, "Recent advances in 3.5μm erbium-doped mid-infrared fiber lasers," *IEEE J. Sel. Topics Quantum Electron.*, vol. 23, no. 3, May/Jun. 2017, Art. no. 0900509.

[6] L. Jun, T. Qiulin, Z. Wendong, X. Chenyang, G. Tao, and X. Jijun, "Miniature low-power IR monitor for methane detection," *Measurement*, vol. 44, no. 5, pp. 823–831, 2011.

[7] D. Richter, A. Fried, B. Wert, J. Walega, and F. Tittel, "Development of a tunable mid-IR difference frequency laser source for highly sensitive airborne trace gas detection," *Appl. Phys. B*, vol. 75, pp. 281–288, 2002.

[8] H. Tobben, "Room temperature CW fibre laser at 3.5 mu m in Er^{3+}-doped ZBLAN glass," *Electron. Lett.*, vol. 14, no. 28, pp. 1361–1362, 1992.

[9] O. Henderson-Sapir, J. Munch, and D. J. Ottaway, "Mid-infrared fiber lasers at and beyond 3.5μm using dual-wavelength pumping," *Opt. Lett.*, vol. 39, no. 3, pp. 493–496, 2014.

[10] M. Lemieux-Tanguay et al., "15 W monolithic fiber laser at 3.55 μm," *Opt. Lett.*, vol. 47, no. 2, pp. 289–292, 2022.

[11] F. Zhou, J. Li, H. Luo, F. Quellette, and Y. Liu, "Numerical analysis of 3.92μm dual-wavelength pumped heavily-holmium-doped fluoroindate fiber lasers," *J. Lightw. Technol.*, vol. 39, no. 2, pp. 633–645, Jan. 2021.

[12] A. M. Loconsole, M. C. Falconi, V. Portosi, and F. Prudenzano, "Numerical design of a gain-switched pulsed laser at 3.92μm wavelength based on a Ho^{3+}-doped fluoroindate fiber," *J. Lightw. Technol.*, vol. 39, no. 10, pp. 3276–3283, May 2021.

[13] J. Cao et al., "Modeling and optimization of cascaded lasing in a holmium doped fluoride fiber laser with efficient output at 3.92 μm," *Opt. Exp.*, vol. 30, no. 18, pp. 31623–31633, 2022.

[14] Z. Zhang et al., "Enhanced 3.9 microm emission from diode pumped Ho^{3+}/Eu^{3+} codoped fluoroindate glasses," *Opt. Lett.*, vol. 46, no. 9, pp. 2031–2034, 2021.

[15] Z. Zhang et al., "Deactivation effects of Tb^{3+} on Ho^{3+} emission in fluoroindate glasses for 3.9μm laser applications," *Ceram. Int.*, vol. 49, no. 8, pp. 12772–12778, 2023.

[16] R. Wang et al., "3.9μm emission and energy transfer in ultra-low OH^-, Ho^{3+} /Nd^{3+} co-doped fluoroindate glasses," *J. Lumin.*, vol. 225, 2020, Art. no. 117363.

[17] A. M. Loconsole, M. C. Falconi, A. Annunziato, S. Cozic, S. Poulain, and F. Prudenzano, "Design of a mid-IR laser based on a Ho: Nd-codoped fluoroindate fiber," *J. Lightw. Technol.*, vol. 41, no. 2, pp. 702–708, Jan. 2023.

[18] L. Gomes, A. F. H. Librantz, F. H. Jagosich, W. A. L. Alves, I. M. Ranieri, and S. L. Baldochi, "Energy transfer rates and population inversion of $^4I_{11/2}$ excited state of Er^{3+} investigated by means of numerical solutions of the rate equations system in Er: LiYF 4 crystal," *J. Appl. Phys.*, vol. 106, no. 10, 2009, Art. no. 103508.

[19] H. Luo, J. Li, J. Li, Y. He, and Y. Liu, "Numerical modeling and optimization of mid-infrared fluoride glass Raman fiber lasers pumped by Tm^{3+}-doped fiber laser," *IEEE Photon. J.*, vol. 5, no. 2, Apr. 2013, Art. no. 2700211.

[20] L. Liu, G.-S. Qin, Q. J. Tian, D. Zhao, and W.-P. Qin, "Numerical investigation of mid-infrared Raman soliton source generation in endless single mode fluoride fibers," *J. Appl. Phys.*, vol. 115, no. 16, 2014, Art. no. 163102.

[21] J. Wang et al., "Numerical modeling of in-band pumped Ho-doped silica fiber lasers," *J. Lightw. Technol.*, vol. 36, no. 24, pp. 5863–5880, Dec. 2018.

[22] F. Maes et al., "Room-temperature fiber laser at 3.92μm," *Optica*, vol. 5, no. 7, pp. 761–764, 2018.

[23] E. Osiac, I. Sokolska, and S. Kück, "Upconversion-induced blue, green and red emission in Ho^{3+}: BaY2F8," *J. Alloys Compounds*, vol. 323, pp. 283–287, 2001.

[24] O. Henderson-Sapir, J. Munch, and D. J. Ottaway, "New energy-transfer upconversion process in Er^{3+}: ZBLAN mid-infrared fiber lasers," *Opt. Exp.*, vol. 24, no. 7, pp. 6869–6883, 2016.

[25] F. Maes et al., "3.42 μm lasing in heavily-erbium-doped fluoride fibers," *Opt. Exp.*, vol. 27, no. 3, pp. 2170–2183, 2019.

[26] J. Schneide, C. Carbonnier, and U. B. Unrau, "Characterization of a Ho^{3+}-doped fluoride fiber laser with a 3.9-μm emission wavelength," *Appl. Opt.*, vol. 36, no. 33, pp. 8595–8600, 1997.

[27] S. Cierullies, H. Renner, and E. Brinkmeyer, "Numerical optimization of multi-wavelength and cascaded Raman fiber lasers," *Opt. Commun.*, vol. 217, no. 1–6, pp. 233–238, 2003.